metals

MDPI

Article

The Relationship of Fracture Mechanism between High Temperature Tensile Mechanical Properties and Particle Erosion Resistance of Selective Laser Melting Ti-6Al-4V Alloy

Jun-Ren Zhao, Fei-Yi Hung *, Truan-Sheng Lui and Yu-Lin Wu

Department of Materials Science and Engineering, National Cheng Kung University, Tainan 701, Taiwan; a2x346yz03@gmail.com (J.-R.Z.); luits@mail.ncku.edu.tw (T.-S.L.); nick22530682@hotmail.com (Y.-L.W.)

* Correspondence: fyhung@mail.ncku.edu.tw; Tel.: +886-6-275-7575 (ext. 62950)

Received: 22 March 2019; Accepted: 26 April 2019; Published: 29 April 2019

Abstract: In this study, selective laser melting (SLM) Ti-6Al-4V is subjected to heat treatment for 4 h at 400 °C, 600 °C, and 800 °C, followed by air cooling. After heat treatment at 400 °C and 600 °C, the ductility was lower (strength increased). This was could be for two reasons: (1) high temperature tensile properties, and (2) particle erosion wear induced phase transformation. Finally, the particle erosion rates of as-SLM Ti-6Al-4V and heat treatment for 4 h at 800 °C (labeled 800-AC) were investigated and compared; the lamellar $\alpha + \beta$ phases in 800-AC are difficult to destroy with erosion particles, resulting in the erosion resistance of 800-AC being higher than that of the martensitic α' needles in the as-SLM Ti-6Al-4V at all impact angles (even the hardness of the 800-AC specimen was lower). The as-SLM Ti-6Al-4V alloy needs heat treatment to have better wear resistance.

Keywords: selective laser melting (SLM); Ti alloy; high temperature tensile; erosion; wear

1. Introduction

Selective laser melting (SLM) process is a type of 3D-printer technology used in this study. The process uses metal powder as a raw material, where during the SLM process, metal powders are melted in a specified area with a high-energy laser beam and rapidly solidified at a high cooling rate [1–3].

Ti-6Al-4V is the most representative of the $\alpha + \beta$ titanium alloys [4,5]. The most common Ti-6Al-4V alloys are cast and forged, and their alloy properties have been widely discussed [6,7]. Many SLM Ti-6Al-4V articles have discussed how process parameters and post treatment interact with microstructure and mechanical properties [8,9]. In this research, the process parameter was fixed. The microstructure of the SLM Ti-6Al-4V contains not only the classical $\alpha + \beta$ phases but also the martensitic α' phases (low ductility) because of the high cooling rate [10,11]. For industrial applications, achieving improved ductility through an appropriate heat treatment is necessary. Furthermore, Ti-6Al-4V is commercially used in gas turbine engines up to a test temperature of 350 ºC. Industrial applications usually limit Ti-6Al-4V use to 400 °C, so high temperature (250–400 °C) tensile mechanical properties of SLM Ti-6Al-4V are investigated in this study and a relationship between the high temperature failure behavior and erosion wear characteristics is proposed.

In many industrial applications, erosion wear caused by solid particles results in the failure of mechanical devices and components [12,13]. This study also investigates erosion properties (use Al_2O_3 particles) between the martensitic α' phase formed by SLM Ti-6Al-4V and the lamellar double $\alpha + \beta$ phases with heat treatment. Notably, the erosion resistance mechanism was proposed by comparing the relationship between impact angles and erosion rate. According to our previous research studies [14,15], the particle erosion wear is able to induce the phase transformation and affects the erosion rate. The temperature of the eroded surface is more than 400 °C, and the relationship between wear behavior and high temperature tensile properties needs to be clarified [16]. This study is one of the few articles discussing the high temperature strength and particle erosion properties of SLM Ti-6Al-4V alloy. The relevant results have significant reference value for relevant 3D-printer titanium alloys.

2. Experimental Procedure

SLM Ti-6Al-4V (the source of the Ti-6Al-4V powder particles is EOS GmbH (Electro-Optical Systems) was used in this study, for which the chemical composition and process parameters are shown in Tables 1 and 2, respectively. The test specimens were removed by the electrical discharge machining (EDM) by cutting the wire from the support, and no post-treatment was implemented before various tests. As-SLM Ti-6Al-4V is called AS in this study. The original test specimens were held for 4 h in a tubular furnace (Deng Yng, new Taipei City, Taiwan) in argon atmosphere at 400 °C, 600 °C, and 800 °C and subjected to air cooling and induced phase transformation. The test specimens were labeled 400-AC, 600-AC, and 800-AC, respectively.

The normal direction (ND) of the specimen was set as parallel to the laser direction, where the direction vertical to the laser direction was called the side direction (SD). After being polished with SiC paper (from #80 to #5000), Al_2O_3 aqueous solution (1 and 0.3 μm), and a 0.04 μm SiO_2 polishing solution, the specimens were etched with Keller's reagent (1 mL HF + 1.5 mL HCL + 2.5 mL HNO_3 + 95 mL H_2O) to examine the microstructure. The microstructure of the specimens was observed using optical microscopy (OM, OLYMPUS BX41M-LED, Tokyo, Japan), and X-ray diffractometry (XRD, Bruker AXS GmbH, Karlsruhe, Germany) was used for identification of the microstructural phases. Hardness measurements were valuated using the Rockwell hardness test (Mitutoyo, Kawasaki-shi, Japan). The measurement conditions for the HR test followed the C-scale (the indenting load 150 kg), and the mean value for five impressions was taken as the hardness of the corresponding condition.

Table 1. Chemical composition of SLM Ti-6Al-4V (wt.%).

Element	Al	V	O	N	C	H	Fe	Ti
wt.%	6.13	3.80	0.20	0.05	0.08	0.01	0.30	Bal.

Table 2. Process parameters of SLM Ti-6Al-4V.

Particle Size (μm)	Laser Power (w)	Laser Radius (μm)	Scanning Velocity (mm/s)	Layer Thickness (μm)
15–45	170	35	800	30

The dimensions of the SLM Ti-6Al-4V tensile specimen are shown in Figure 1. The tensile test was performed with an universal testing machine (HT-8336, Hung Ta, Taichung, Taiwan), with the crosshead speed at 1 mm/min, which corresponded to the initial strain rate of 18.33×10^{-4} s^{-1}. The AS and the heat-treated different temperatures specimens were subjected to a room temperature tensile test to analyze the mechanical properties of SLM Ti-6Al-4V. There were at least three specimens for each test and the mean value of the test specimens was taken as the tensile results of the corresponding condition.

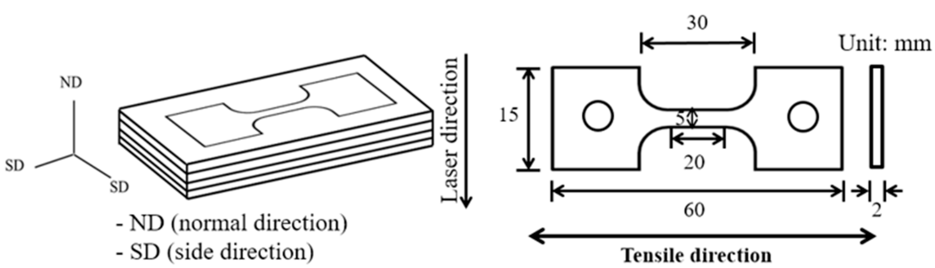

Figure 1. Dimensions of the selective laser melting (SLM) Ti-6Al-4V tensile specimen.

Regarding the high temperature tensile properties, titanium alloys are often applied in a high temperature environment of 250–400 °C [17]; therefore, tensile tests were carried out at 250 °C, 300 °C, 350 °C, and 400 °C to investigate the influence of temperature on the mechanical properties of SLM Ti-6Al-4V. There are at least three specimens for each test and the mean value of the test specimens was taken as the tensile results of the corresponding condition.

The equipment used in the erosion test is shown in Figure 2. Al_2O_3 particles were used, for which the average particle size was approximately 450 μm and scanning electron microscope (SEM) morphology is shown in Figure 3. The specimens were polished with #80 to #1000 SiC papers to remove the oxidized layer and soaked in acetone for ultrasonic cleaning before the erosion test. Then, 200 g of the erosion particles under a compressed air flow of 3 kg/cm^2 (0.29 MPa) were subjected to the erosion test [14,15], for which the impact angles were 15°, 30°, 45°, 60°, 75°, and 90° to compare the erosion behavior of needle-like α' phase in the AS specimen and the plate-like $\alpha + \beta$ phase in 800-AC specimen. According to previous reports, the maximum erosion rate of the general ductile material takes place at about 20°–30°, but brittle materials, such as ceramics and glass, have maximum erosion rates at about 90° [14,15]. The erosion rate ($ER\% = \delta W/W_{total\ particles}$) of a specimen is defined as its weight loss (δW) divided by the weight of the total erosion particles ($W_{total\ particles}$). Finally, optical microscopy and a scanning electron microscope (SEM, HITACHI SU-5000, HITACHI, Tokyo, Japan) were used to examine the surface and subsurface of the erosion specimens and to determine the erosion mechanism. All heat treatment conditions and measurements are shown in Table 3.

Table 3. Heat treatment condition and measurements.

Sample	Heat Treatment Condition	Room Temperature Tensile Test	High Temperature Tensile Test	Particles Erosion Test
AS	-	✓	✓	✓
400-AC	400 °C/4 h → air cooling	✓	-	-
600-AC	600 °C/4 h → air cooling	✓	-	-
800-AC	800 °C/4 h → air cooling	✓	-	✓

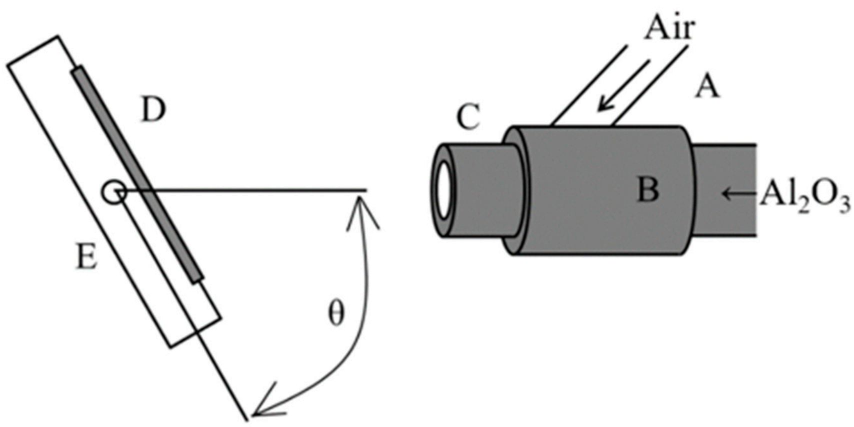

Figure 2. The particle erosion test apparatus. (**A**) Compressed air flow, (**B**) erosion particle supplier, (**C**) erodent nozzle, (**D**) specimen, and (**E**) specimen holder; θ = impact angle.

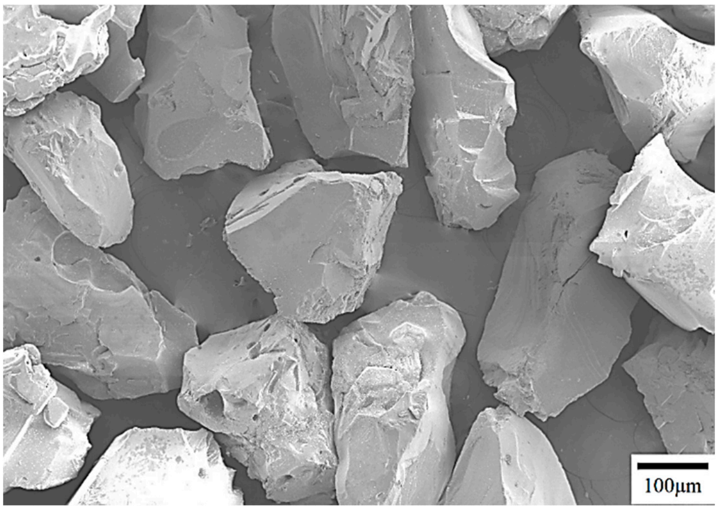

Figure 3. Scanning electron microscope (SEM) morphology of Al_2O_3 erosion particles.

3. Results and Discussion

3.1. Microstructures and Phases

Figure 4 shows the microstructures of the as-SLM Ti-6Al-4V subjected to heat treatment at different holding temperatures. Figure 4a shows the normal direction microstructure of AS, where it can be observed that a large number of needle-like phases are surrounded by a network profile with a diameter of approximately 80 μm. Figure 4b shows the same needle-like structure, therefore the AS is a needle-like structure as a whole. The normal direction and side direction microstructures were subjected to heat treatment at 400 °C for 4 h, as shown in Figure 4c,d, respectively. The microstructure of 400-AC is similar to that of AS, which is comprised of needle-like α′ phases as a whole. Similar microstructures can also be seen at 600-AC, as shown in Figure 4e,f. In addition, white plate-like α phases were produced at 600 °C. Figure 4g,h shows that the microstructure of 800-AC is different from that of AS, 400-AC, and 600-AC. At 800 °C, a significant phase transformation occurred, and the α′ phases disappeared and were substituted with continuous lamellar α + β phases comprising white α phases surrounded by black β phases.

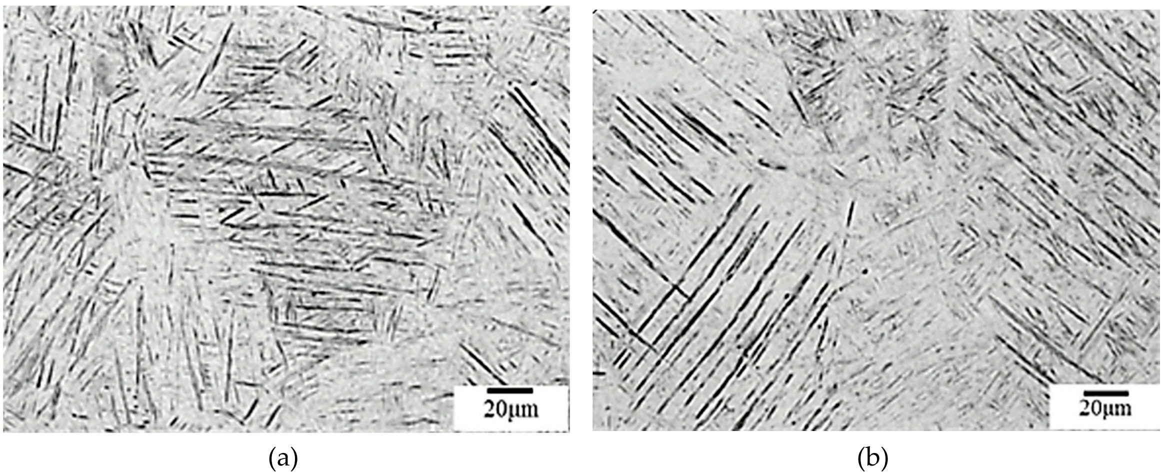

Figure 4. *Cont.*

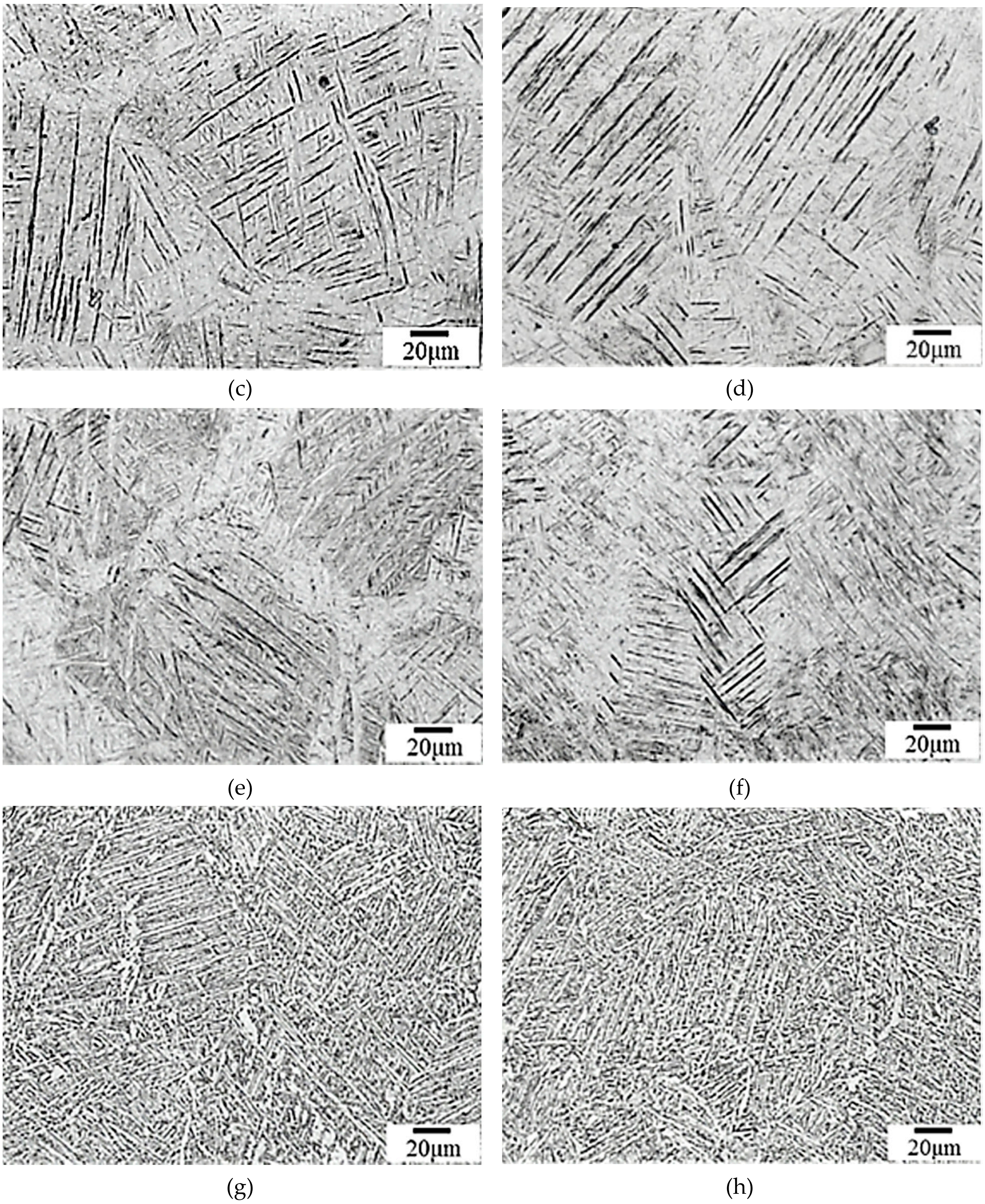

Figure 4. Microstructures in the (**a**) normal direction of as-SLM Ti-6Al-4V (AS), (**b**) side direction of AS, (**c**) normal direction of 400-AC, (**d**) side direction of 400-AC, (**e**) normal direction of 600-AC, (**f**) side direction of 600-AC, (**g**) normal direction of 800-AC, and (**h**) side direction of 800-AC.

The β peak at 600 °C and the presence of the α/α′and β peaks at 800 °C were confirmed with a XRD analysis, as shown in Figure 5. The XRD patterns are referenced from a previous report [18]. This indicates that when the heat treatment temperature increases up to 600 °C, the β-phase will be generated. According to a previous report [19,20], as shown in Figures 4 and 5, there is only an α′ phase in AS. The equiaxed β phases were preferentially formed above the β-transform temperature during the cooling process. Because of the extremely high temperature gradient in quenching [21,22], the β phases were completely transformed into the needle-like martensitic α′ phase. According to the Xu et al. report [19], when the AS specimen was heated to 400 °C, the α phases were precipitated, where the phase transformation mechanism was α′ → α′ + α. When AS specimen is heated to 600 °C, the temperature is higher than the martensitic transformation temperature (575 °C), plate-like α phases precipitate around the α′ phases, and a small amount of β phases precipitate on the α phase boundaries as hold time increases, where the mechanism of phase transformation is α′ → α′ + α + β. When AS specimen is heated to 800 °C, the α′ phases completely disappear, and transformation to the continuous lamellar α + β phase occurs, for which the phase transformation mechanism is α′ → α + β.

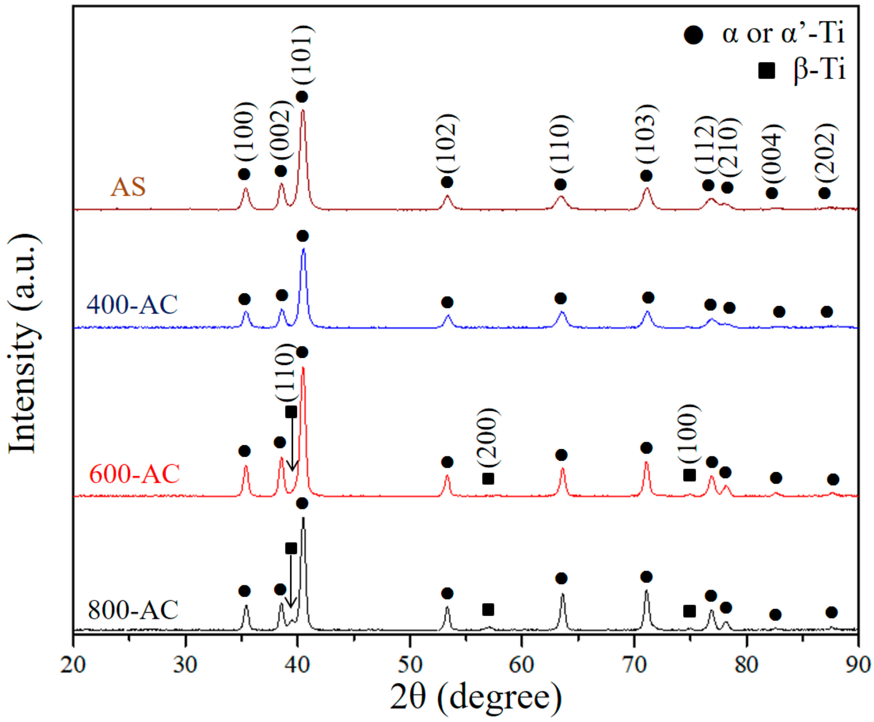

Figure 5. X-ray diffraction pattern of AS, 400-AC, 600-AC, and 800-AC specimens.

3.2. Mechanical Properties

Figure 6 shows the hardness (normal direction) comparison of AS, 400-AC, 600-AC, and 800-AC. The hardness of AS, 400-AC, and 600-AC is similar, but when the heat treatment temperature increases up to 800 °C, the hardness decreases because α′ phases are completely transformed into α + β phases.

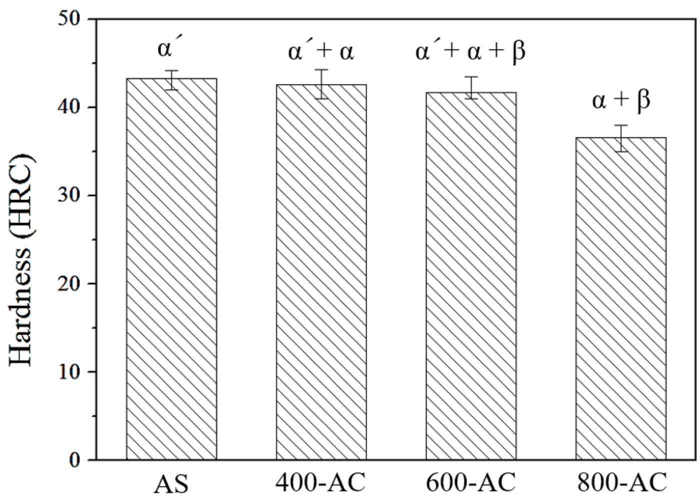

Figure 6. Hardness of AS, 400-AC, 600-AC, and 800-AC (normal direction).

The room temperature tensile properties of AS, 400-AC, 600-AC, and 800-AC are shown in Figure 7, with the mean value of the mechanical properties list in Table 4. It can be seen that the strength of 400-AC is significantly higher than that of AS. According to previous reports [23,24], the tensile strength can be improved by the precipitation of α phases in the grains or on the boundaries, and the residual stress is also reduced by a 400 °C heat treatment, so the strength of 400-AC is higher than that of AS.

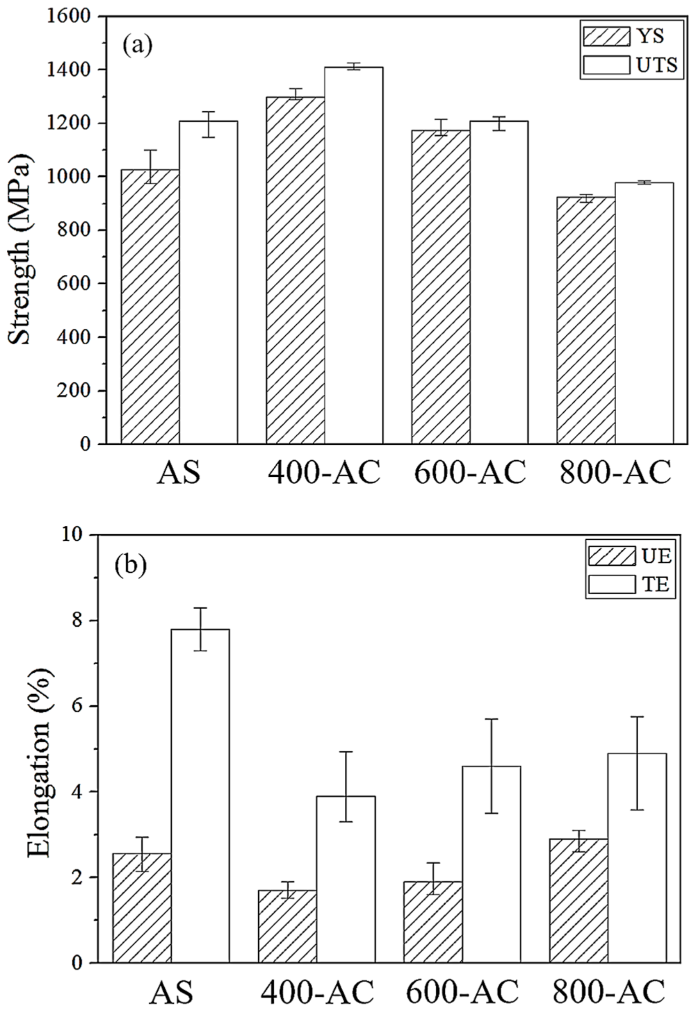

Figure 7. Tensile properties of AS, 400-AC, 600-AC, and 800-AC at room temperature for (**a**) strength and (**b**) ductility.

Table 4. Room temperature tensile properties of AS, 400-AC, 600-AC, and 800-AC. (YS: yield strength; UTS: ultimate tensile strength; UE: uniform elongation; TE: total elongation).

Test Specimen	YS (MPa)	UTS (MPa)	UE (%)	TE (%)
AS	1025	1210	2.6	7.8
400-AC	1300	1410	1.7	3.9
600-AC	1175	1210	1.9	4.6
800-AC	925	980	2.9	4.9

The β phases begin to precipitate, and the strength gradually decreases with increases in the heat treatment temperature, and the strength is similar to AS at 600 °C, but the strength at 800 °C is lower than that of AS because the α′ phases are completely transformed into the α + β phases. On the other hand, the ductility increases as the heat treatment temperature increases, but is still less than 10% and less than that of AS. The precipitation of the α phases increases the strength but significantly decreases the ductility. Increases in the ductility are attributed to the formation of β phases, and α′ phases are completely transformed into α + β phases upon increases in the heat treatment temperature. In other words, the precipitation of the α phases contributes to the improvement of tensile strength, where the increase in ductility can be attributed to the formation of the β phases.

Figure 8 shows the morphology of the tensile fracture surfaces of AS, 400-AC, 600-AC, and 800-AC at room temperature. Dimpled ductility structures can be observed in all specimens. In addition, some cleavage facets can be observed in 400-AC, which is consistent with its low ductility.

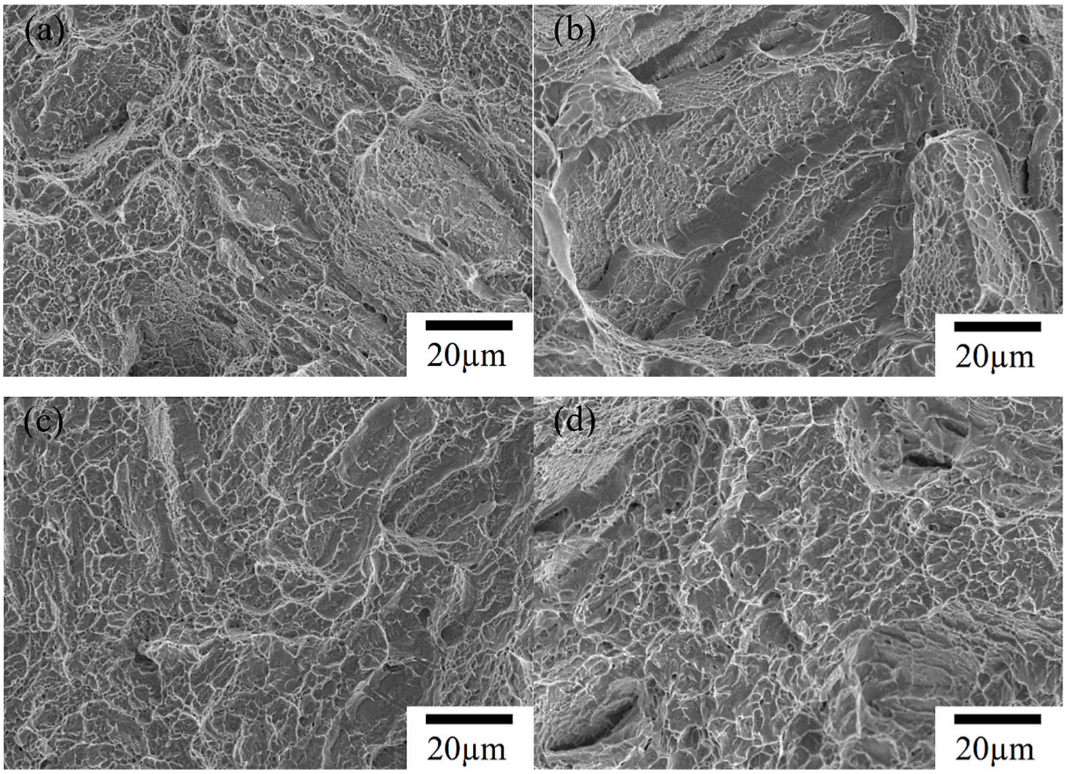

Figure 8. Morphologies of tensile fracture surfaces at room temperature for (**a**) AS, (**b**) 400-AC, (**c**) 600-AC, and (**d**) 800-AC.

Figure 9 shows the high temperature tensile properties of AS, and the mean value of the mechanical properties is listed in Table 5. The strength decreases slowly as the temperature increases. The UTS is close to 1000 MPa and the YS is about 800 MPa at 400 °C, indicating that the phase transformation α′→ α + β is exhibiting decreased strength. Compared to previous reports [25,26], the strength of commercial Ti-6Al-4V has a dramatic decrease whilst the temperature increases. Apparently the as-SLM Ti-6Al-4V could maintain a certain strength under 400 °C. In terms of ductility, there is first an increasing and then a decreasing trend, with the total elongation (TE) close to 10% at 250 °C–300 °C, which means the 3D-printer titanium alloy can be used in medium temperature applications. It is worth noting that the ductility at 400 °C is similar to that of AS, which implies that it is affected by a small α phase precipitation effect. In summary, the tensile properties of 350 °C are most applicable with the highest values in uniform elongation (UE). Figure 10 shows macroscopic morphology photographs of high temperature tensile fracture specimens, though there is not an obvious shrinkage phenomenon in any of the specimens, and there is no hole expansion at the location of the inserted pin. The macroscopic fracture morphology becomes gradually flatter from a zigzag pattern as the tensile temperature increases.

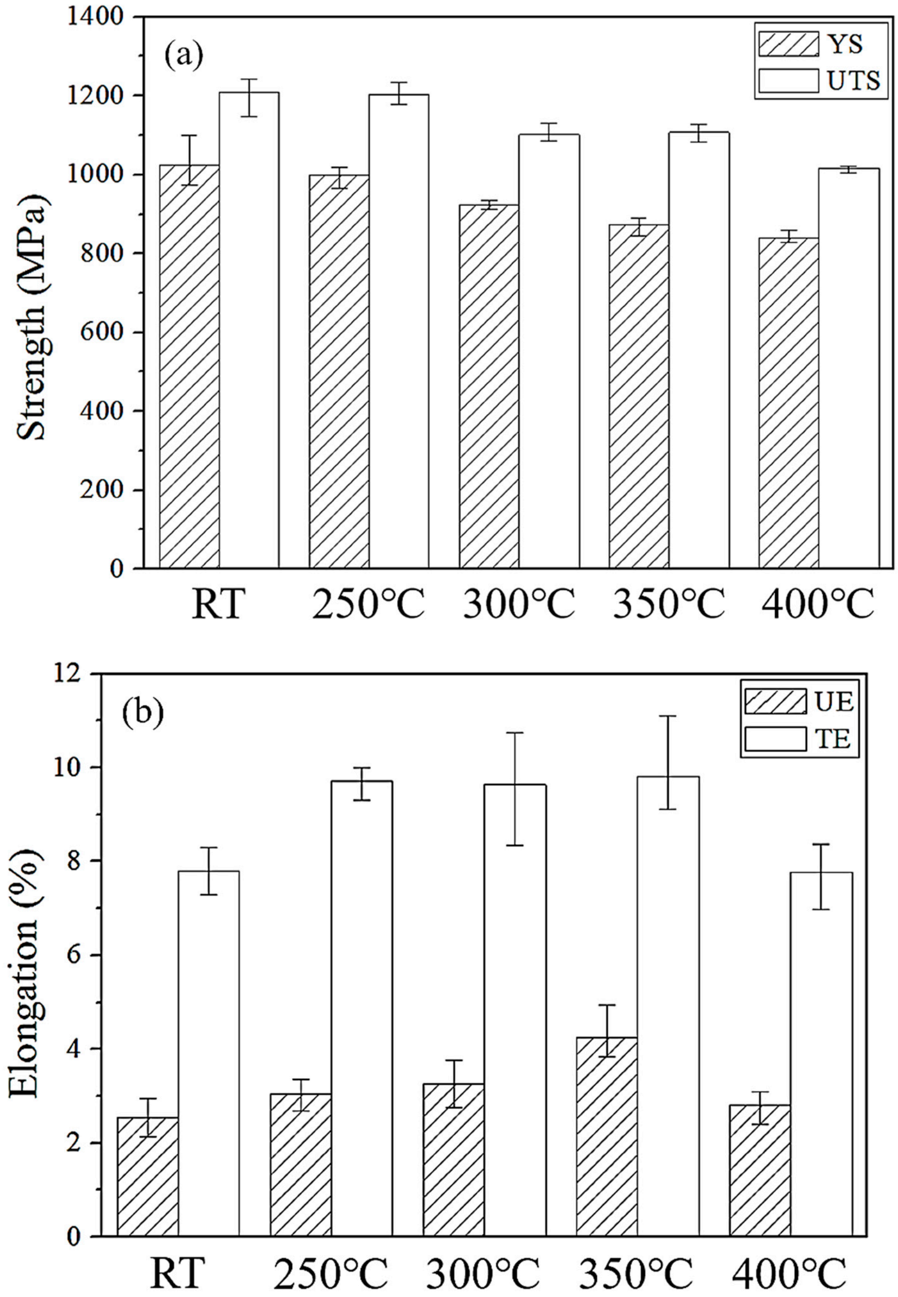

Figure 9. High temperature tensile properties of AS for (**a**) strength and (**b**) ductility.

Table 5. High temperature tensile properties of AS.

Test Specimen	YS (MPa)	UTS (MPa)	UE (%)	TE (%)
AS	1025	1210	2.6	7.8
250 °C	1000	1203	3.1	9.7
300 °C	923	1102	3.3	9.6
350 °C	873	1107	4.3	9.8
400 °C	839	1016	2.8	7.8

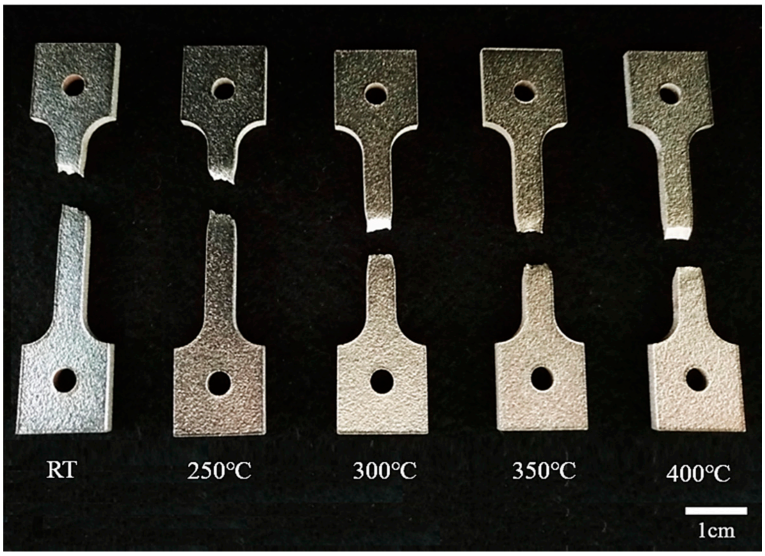

Figure 10. Macroscopic morphology photographs of room temperature and high temperature tensile fracture specimens.

3.3. Particle Erosion Characteristics and Mechanisms

In order to clarify the difference in erosion characteristics of different matrices, this study chose AS and 800-AC specimens exhibiting erosion for comparison. Figure 11 shows the erosion data of AS and 800-AC eroded by Al_2O_3 particles; there are at least three specimens for each test and the mean value of the test specimens was taken as the erosion results of the corresponding condition. The reason for using AS for comparison with 800-AC was due to the fact that the martensitic α' phases of AS were completely transformed into the lamellar $\alpha + \beta$ phases, where the ratio α:β was about 68:32. Because AS and 800-AC exhibited completely different microstructures, the effects of the phase difference on the erosion wear properties could be fully investigated. Notably, both AS and 800-AC had maximum erosion rates at 30° impact, where the erosion rates decreased with increases in the impact angle, and the minimum erosion rate at a 90° impact resulted in ductile-cutting dominating the erosion behavior. At all impact angles, the erosion rate of AS was greater than that of 800-AC, indicating the erosion resistance of the continuous lamellar $\alpha + \beta$ phases of 800-AC were better than that of AS. The erosion resistance was positively correlated with the hardness of conventional Ti-6Al-4V alloy [27], but the result was different in this research. The difference in microstructure caused this result, therefore we investigated the surface and subsurface morphologies of AS and 800-AC at different impact angles.

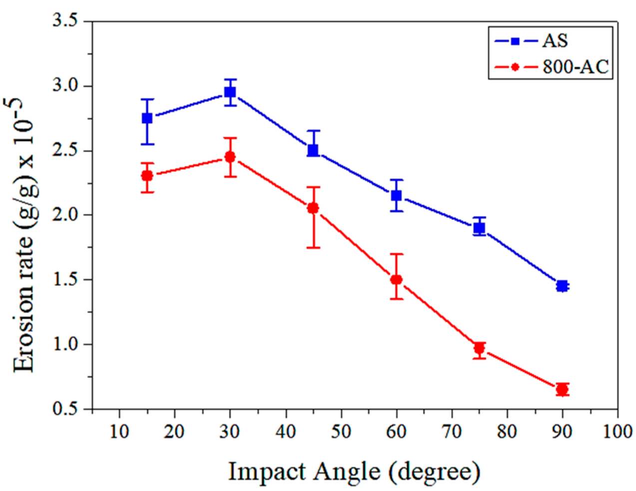

Figure 11. The erosion rate as a function of the impact angles of AS and 800-AC.

Figure 12a shows the surface morphology of AS at 30° impact, where lips and grooving can be seen on the surface. Figure 12b shows the surface morphology of AS at 90° impact, where pits formed by erosion wear can be seen. Figure 12c shows the surface morphology of 800-AC at 30° impact, where compared with the lips on the AS surface, the surface morphology of 800-AC was completely cut by erosion particles and the lips of the erosion subsurface were smaller. Figure 12d shows the surface morphology of 800-AC at 90° impact, where pits formed by erosion wear can also be seen, similar to AS. However, some scratch marks could also be observed on the surface of 800-AC at 90° impact. This phenomenon indicated that the specimen was deformed by squeezing first and then was stripped by the erosion particles.

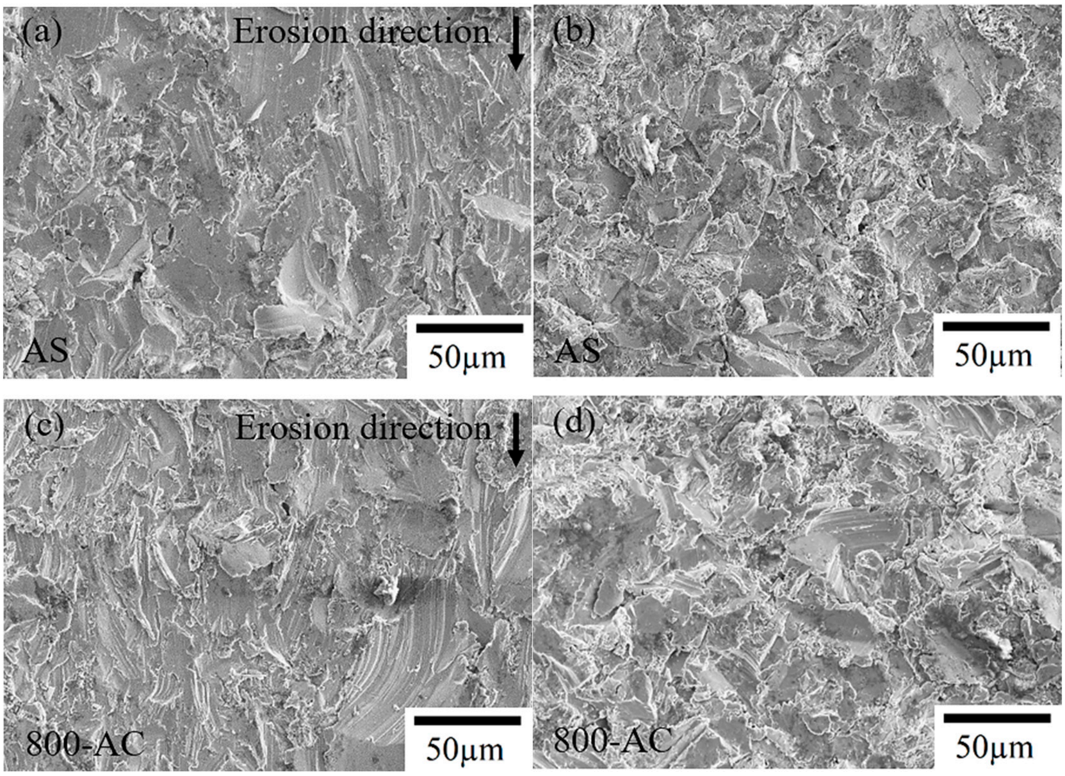

Figure 12. Surface morphologies of AS at (**a**) 30° and (**b**) 90°. Surface morphologies of 800-AC at (**c**) 30° and (**d**) 90°.

Figure 13a shows subsurface morphologies of AS at 30° impact, where lips caused by erosion particles can be found on the subsurface in the circled area. Figure 13b shows subsurface morphologies of AS at 90° impact, where both narrow and deep pits can be observed, and subsurface morphologies of 800-AC at 30° impact, where almost no lips can be observed (Figure 13c). They are replaced by smoother features resulting from erosion particles. Figure 13d shows the subsurface morphologies of 800-AC at 90° impact, where the pits that can be observed in 800-AC are wider and shallower than those in AS. Notably, the surface roughness of erosion subsurface is lower than that of AS-90° impact.

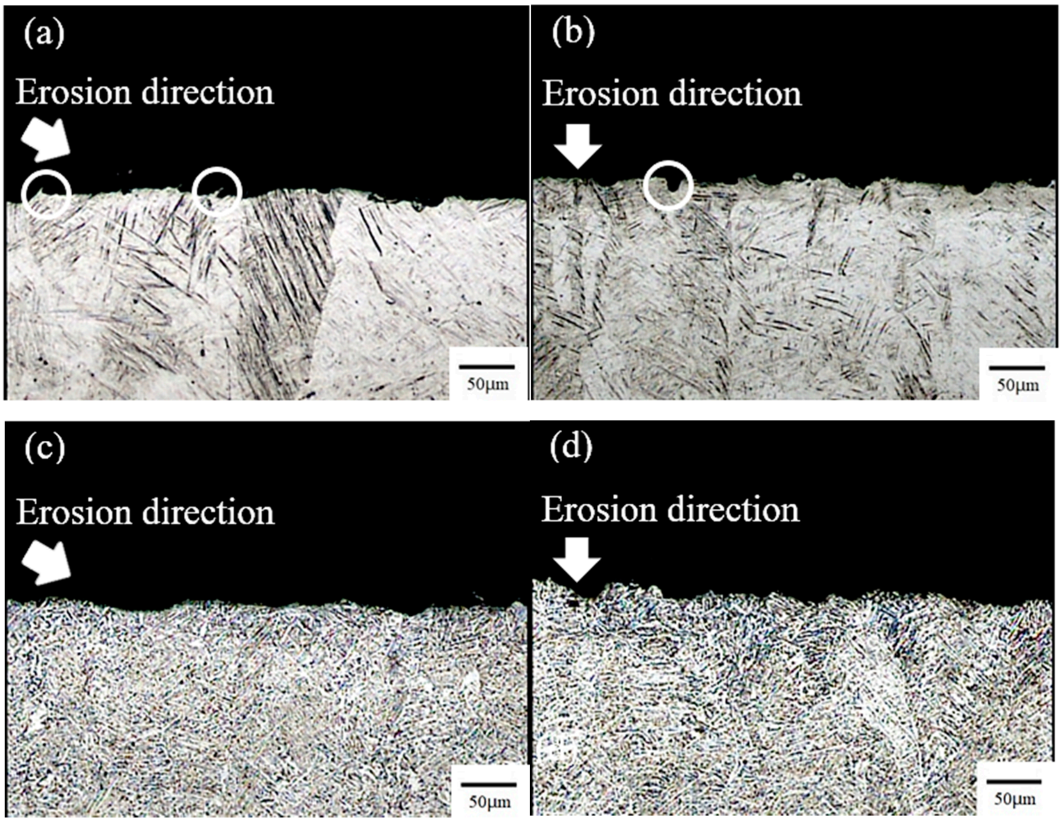

Figure 13. Subsurface morphologies of AS at (**a**) 30° and (**b**) 90°. Surface morphologies of 800-AC at (**c**) 30° and (**d**) 90°.

Figure 14 provides the erosion mechanism schematic diagrams of AS and 800-AC at impacts of 30° and 90°, respectively. Figure 14a is the erosion mechanism of AS at 30° impact, where it can be seen that due to the inability of the needle-like martensitic α' phases to prevent erosion wear due to erosion particles, the lips are formed by the cutting mechanism. When AS is eroded by erosion particles at 90° impact, the surface of the specimen is subjected to the positive impact of erosion particles, which form squeeze features on the erosion wear surface, but the positive impact resistance of AS is weaker than that of 800-AC, thus resulting in the formation of deeper pits, as shown in Figure 14b. When the 800-AC is inclined and eroded by erosion particles at 30° impact, the lamellar $\alpha + \beta$ phases process smaller and fewer lips, as shown in Figure 14c. Figure 14d shows the erosion wear behavior of 800-AC at 90° impact, where some of the continuous lamellar $\alpha + \beta$ phases are scraped off when the erosion particles have a positive impact. However, the damage characteristics are not significant.

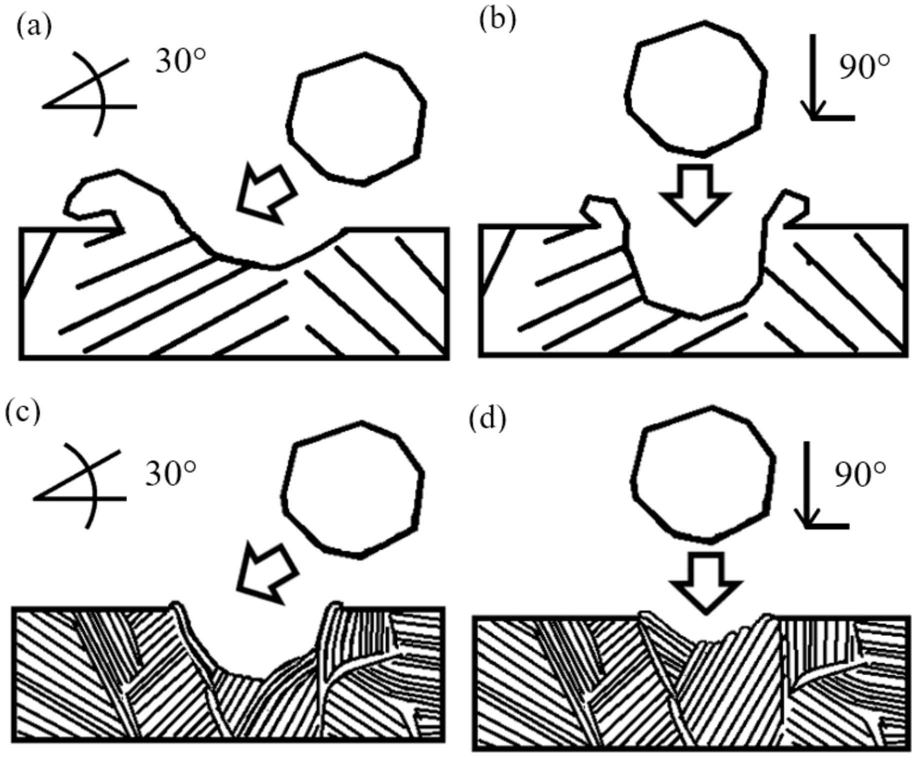

Figure 14. Particle erosion mechanism of AS at (**a**) 30° and (**b**) 90°. Particle erosion mechanism of 800-AC at (**c**) 30° and (**d**) 90°.

According to the discussion above regarding the eroded surface morphology, including the subsurface morphology of the erosion and the erosion mechanism, although the ductility of 800-AC was not as good as that of AS, its continuous lamellar $\alpha + \beta$ phases were tough enough to limit the ability of the erosion particles to scrape off the material at all impact angles. Thus, the erosion resistance of 800-AC was determined to be better than that of AS. The SLM Ti-6Al-4V specimen must be heat treated to have wear resistance.

4. Limitations

The particle erosion induced phase transformation on 3D titanium alloy needs further investigation and analysis.

5. Conclusions

(1) The microstructure of as-SLM Ti-6Al-4V appears as a needle-like martensitic α' phase. Depending on different heat treatment temperatures, there are different phase compositions. The phase composition of 400 °C is $\alpha' + \alpha$, 600 °C is $\alpha' + \alpha + \beta$, and at 800 °C, the α' phase is completely transformed into the lamellar $\alpha + \beta$ phases. The phase composition of 800-AC is $\alpha + \beta$.

(2) For the SLM Ti-6Al-4V specimen, the high temperature strength decreases as the temperature continues to increase after 400 °C, and the ductility increases as the temperature rises. The as-SLM Ti-6Al-4V could maintain a certain strength under 400 °C. Among the specimens, the highest UE is at 350 °C, so the tensile properties at 350 °C are most appropriate for the application of interest.

(3) Both AS and 800-AC had maximum erosion rates at 30° impact, and minimum erosion rates at 90° impact, where ductile failure dominated the erosion behavior. The continuous lamellar α + β phases of 800-AC were tough enough to limit the ability of the erosion particles to scrape off the material at all impact angles.

Author Contributions: Methodology, J.-R.Z. and Y.-L.W.; investigation, J.-R.Z. and Y.-L.W.; data curation, J.-R.Z.; writing—original draft preparation, J.-R.Z.; writing—review and editing, F.-Y.H. and T.-S.L.; supervision, F.-Y.H. and T.-S.L.

Funding: This research received no external funding.

Acknowledgments: The authors are grateful to The Instrument Center of National Cheng Kung University and the Ministry of Science and Technology of Taiwan (Grant No. MOST 107-2221-E-006-012-MY2) for their financial support for this research.

Conflicts of Interest: The authors declare no conflict of interest.

References

1. Yadroitsev, I.; Krakhmalev, P.; Yadroitsava, I. Selective laser melting of Ti6Al4V alloy for biomedical applications: Temperature monitoring and microstructural evolution. *J. Alloy Compd.* **2014**, *583*, 404–409. [CrossRef]
2. Song, B.; Dong, S.; Liao, H.; Coddet, C. Process parameter selection for selective laser melting of Ti6Al4V based on temperature distribution simulation and experimental sintering. *Int. J. Adv. Manuf. Technol.* **2012**, *61*, 967–974. [CrossRef]
3. Kelly, C.N.; Evans, N.T.; Irvin, C.W.; Chapman, S.C.; Gall, K.; Safranski, D.L. The effect of surface topography and porosity on the tensile fatigue of 3D printed Ti-6Al-4V fabricated by selective laser melting. *Mater. Sci. Eng. C* **2019**, *98*, 726–736. [CrossRef]
4. Ahmadi, M.; Karpat, Y.; Acar, O.; Kalay, Y.E. Microstructure effects on process outputs in micro scale milling of heat treated Ti6Al4V titanium alloys. *J. Mater. Process. Tech.* **2018**, *252*, 333–347. [CrossRef]
5. Oh, S.T.; Woo, K.D.; Kim, J.H.; Kwak, S.M. The Effect of Al and V on Microstructure and Transformation of β Phase during Solution Treatments of Cast Ti-6Al-4V Alloy. *Korean J. Met. Mater.* **2017**, *55*, 150–155.
6. Zhang, Z.X.; Qu, S.J.; Feng, A.H.; Hu, X.; Shen, J. Microstructural mechanisms during multidirectional isothermal forging of as-cast Ti-6Al-4V alloy with an initial lamellar microstructure. *J. Alloy Compd.* **2019**, *773*, 277–287. [CrossRef]
7. Matsumoto, H.; Velay, V. Mesoscale modeling of dynamic recrystallization behavior, grain size evolution, dislocation density, processing map characteristic, and room temperature strength of Ti-6Al-4V alloy forged in the (α + β) region. *J. Alloy Compd.* **2017**, *708*, 404–413. [CrossRef]
8. Khorasani, A.; Gibson, I.; Awan, U.S.; Ghaderi, A. The effect of SLM process parameters on density, hardness, tensile strength and surface quality of Ti-6Al-4V. *Addit. Manuf.* **2019**, *25*, 176–186. [CrossRef]
9. Wang, Z.; Xiao, Z.; Tse, Y.; Huang, C.; Zhang, W. Optimization of processing parameters and establishment of a relationship between microstructure and mechanical properties of SLM titanium alloy. *Opt. Laser. Technol.* **2019**, *112*, 159–167. [CrossRef]
10. Sun, J.; Yang, Y.; Wang, D. Parametric optimization of selective laser melting for forming Ti6Al4V samples by Taguchi method. *Opt. Laser. Technol.* **2013**, *49*, 118–124. [CrossRef]
11. Song, B.; Dong, S.; Zhang, B.; Liao, H.; Coddet, C. Effects of processing parameters on microstructure and mechanical property of selective laser melted Ti6Al4V. *Mater. Design.* **2012**, *35*, 120–125. [CrossRef]
12. Dai, W.S.; Chen, L.H.; Lui, T.S. A study on SiO_2 particle erosion of flake graphite and spheroidal graphite cast irons. *Wear* **2000**, *239*, 143–152. [CrossRef]
13. Cai, F.; Huang, X.; Yang, Q. Mechanical properties, sliding wear and solid particle erosion behaviors of plasma enhanced magnetron sputtering CrSiCN coating systems. *Wear* **2015**, *324–325*, 27–35. [CrossRef]
14. Liou, J.W.; Lui, T.S.; Chen, L.H. SiO_2 particle erosion of A356.2 aluminum alloy and the related microstructural changes. *Wear* **1997**, *211*, 169–176. [CrossRef]
15. Hung, F.Y.; Chen, L.H.; Lui, T.S. Phase Transformation of an Austempered Ductile Iron during an Erosion Process. *Mater. Trans.* **2004**, *45*, 2981–2986. [CrossRef]
16. Chen, H.; Xu, C.; Chen, J.; Zhao, H.; Zhang, L.; Wang, Z. Microstructure and phase transformation of WC/Ni60B laser cladding coatings during dry sliding wear. *Wear* **2008**, *264*, 487–493. [CrossRef]
17. Baitimerov, R.M.; Lykov, P.A.; Radionova, L.V.; Akhmedianov, A.M.; Samoilov, S.P. An investigation of high temperature tensile properties of selective laser melted Ti-6Al-4V. In Proceedings of the 3rd International Conference on Progress in Additive Manufacturing (Pro-AM 2018), Nanyang Technological University, Singapore, 14–17 May 2018.

18. Da Silva, S.L.R.; Kerber, L.O.; Amaral, L.; dos Santos, C.A. X-ray diffraction measurements of plasma-nitrided Ti–6Al–4V. *Surf Coat Tech.* **1999**, *116–119*, 342–346. [CrossRef]
19. Xu, W.; Brandt, M.; Sun, S.; Elambasseril, J.; Liu, Q.; Latham, K.; Xia, K.; Qian, M. Additive manufacturing of strong and ductile Ti–6Al–4V by selective laser melting via in situ martensite decomposition. *Acta Mater.* **2015**, *85*, 74–84. [CrossRef]
20. Thijs, L.; Verhaeghe, F.; Craeghs, T.; Humbeeck, J.V. A study of the microstructural evolution during selective laser melting of Ti-6Al-4V. *Acta Metall.* **2010**, *58*, 3303–3312. [CrossRef]
21. Lütjering, G. Influence of processing on microstructure and mechanical properties of (α + β) titanium alloys. *Mate. Sci. Eng. A* **1998**, *243*, 32–45. [CrossRef]
22. Do, D.K.; Li, P. The effect of laser energy input on the microstructure, physical and mechanical properties of Ti-6Al-4V alloys by selective laser melting. *Virtual Phys. Prototyping* **2016**, *11*, 41–47. [CrossRef]
23. Tao, P.; Li, H.X.; Huang, B.Y.; Hu, Q.D.; Gong, S.L.; Xu, Q.Y. Tensile behavior of Ti-6Al-4V alloy fabricated by selective laser melting: Effects of microstructures and as-built surface quality. *Chin. Foundry* **2018**, *15*, 243–252. [CrossRef]
24. Vrancken, B.; Thijs, L.; Kruth, J.P.; Humbeeck, J.V. Heat treatment of Ti-6Al-4V produced by Selective Laser Melting: Microstructure and mechanical properties. *J. Alloys Compd.* **2012**, *541*, 177–185. [CrossRef]
25. Bush, R.W.; Brice, C.A. Elevated temperature characterization of electron beam freeform fabricated Ti–6Al–4V and dispersion strengthened Ti–8Al–1Er. *Mater. Sci. Eng. A* **2012**, *554*, 12–21. [CrossRef]
26. Kim, J.; Kim, K.H.; Kwon, D. Evaluation of High-Temperature Tensile Properties of Ti-6Al-4V Using Instrumented Indentation Testing. *Met. Mater. Int.* **2016**, *22*, 209–215. [CrossRef]
27. Sahoo, R.; Mantry, S.; Sahoo, T.K.; Mishra, S.; Jha, B.B. Effect of Microstructural Variation on Erosion Wear Behavior of Ti-6Al-4V Alloy. *Tribol. Trans.* **2013**, *56*, 555–560. [CrossRef]